Integrating proteomic data with metabolic modelling provides insight into key pathways of *Bordetella pertussis* biofilms

Hiroki Suyama[1], Laurence Don Wai Luu[1], Ling Zhong[2], Mark J. Raftery[2] and Ruiting Lan[1*]

[1]School of Biotechnology and Biomolecular Sciences, University of New South Wales, Sydney, New South Wales, Australia

[2]Bioanalytical Mass Spectrometry Facility, University of New South Wales, Sydney, New South Wales, Australia

*Corresponding Author

Email: r.lan@unsw.edu.au

Phone: 61-2-9385 2095

Fax: 61-2-9385 1483

Abstract

Pertussis, commonly known as whooping cough is a severe respiratory disease caused by the bacterium, *Bordetella pertussis*. Despite widespread vaccination, pertussis resurgence has been observed globally. The development of the current acellular vaccine (ACV) has been based on planktonic studies. However, recent studies have shown that *B. pertussis* readily forms biofilms. A better understanding of *B. pertussis* biofilms is important for developing novel vaccines that can target all aspects of *B. pertussis* infection. This study compared the proteomic expression of biofilm and planktonic *B. pertussis* cells to identify key changes between the conditions. Major differences were identified in virulence factors including an upregulation of toxins (adenylate cyclase toxin and dermonecrotic toxin) and downregulation of pertactin and type III secretion system proteins in biofilm cells. To further dissect metabolic pathways that are altered during the biofilm lifestyle, the proteomic data was then incorporated into a genome scale metabolic model using the integrated metabolic analysis tool (iMAT). The analysis revealed that planktonic cells utilised the glyoxylate shunt while biofilm cells completed the full tricarboxylic acid cycle. Differences in processing aspartate, arginine and alanine were identified as well as unique export of valine out of biofilm cells which may have a role in inter-bacterial communication and regulation. Finally, increased polyhydroxybutyrate accumulation and superoxide dismutase activity in biofilm cells may contribute to increased persistence during infection. Taken together, this study modelled major proteomic and metabolic changes that occur in biofilm cells which helps lay the groundwork for further understanding *B. pertussis* pathogenesis.

36 **Introduction**

37 Whooping cough is a re-emerging severe respiratory disease caused by *Bordetella*
38 *pertussis*. Following the change from the whole cell vaccine (WCV) to the acellular vaccine
39 (ACV) in many developed countries, there has been an increase in the incidence of whooping
40 cough (1-4). Although most likely multifaceted, waning immunity of the ACV and vaccine
41 driven selection of non-ACV genotypes or strains not expressing one of the ACV antigens
42 have been previously reported as major factors contributing to the re-emergence of pertussis
43 (5, 6). It is evident that an improved ACV is needed to control the infections.

44 Recent studies have shown that *B. pertussis* readily forms biofilms *in vivo* (7-10).
45 Development of the vaccine has been based on planktonic studies and may not be entirely
46 representative of the infection cycle. Although proteomic comparisons have been performed
47 between biofilm and planktonic *B. pertussis* cells (11-13), little is known about the metabolic
48 reactions that are altered while in the biofilm state. In response to changes in environment,
49 the most widely studied regulator of gene expression in *B. pertussis* is the *Bordetella*
50 virulence gene (Bvg) system (14). The Bvg system controls the expression of most of the
51 virulence factors in *B. pertussis* but has also been implicated in the regulation of metabolism
52 (15). The Bvg system exists in 3 states, Bvg^+, Bvg^- and Bvg^i where the expression of
53 virulence genes is active, inactive or intermediately expressed, respectively. There are
54 conflicting studies surrounding the role of the Bvg system in the biofilm process, but studies
55 have linked *Bordetella* biofilm with the Bvg^i phase (11). Further studies identifying key
56 changes in protein expression and metabolism in biofilm cells can provide an insight into the
57 capabilities of the pathogen and help with understanding the role of biofilms in *B. pertussis*
58 pathogenesis.

59 Genome scale metabolic models (GSMM) have emerged as a powerful tool in
60 understanding the metabolic capabilities of an organism. The creation of a GSMM begins as
61 a draft network based on annotated enzyme data and the genome. This yields a model with a
62 network of reactions and metabolites within a mathematical matrix. The movement of
63 metabolites through the network is defined as flux i.e. the rate at which the metabolites are
64 consumed or produced. Based on stoichiometric and thermodynamic constraints, permissible
65 minimum and maximum flux values for each reaction can be calculated (16).

66 GSMMs have been successfully utilised in several pathogens such as *Salmonella*
67 *enterica* serovar Typhimurium (17), *Listeria monocytogenes* (18, 19), *Staphylococcus aureus*
68 (20) and *Mycobacterium tuberculosis* (21) to predict important pathways for virulence and
69 growth. Currently, there have been over 6,000 organisms that have been metabolically
70 reconstructed either manually or automatically (22). There have been two GSMMs
71 extensively curated for *B. pertussis* (23, 24). These models showed the metabolic versatility
72 of the organism by identifying minimal nutrient requirements. Additionally, both models
73 were utilised to validate key pathways essential for infection (25). The major drawback of
74 these models is the assumption that all protein products are simultaneously expressed. Many
75 physical and chemical constraints make this assumption unlikely to be true. Additionally, the
76 different conditions in which the organism is grown strongly affects the metabolic processes
77 (26). To predict metabolic reactions reflecting a specific phenotype, such as biofilms, a
78 context specific model should be created. This can be done through the integration of 'omics'
79 expression data into the GSMM to enrich pathways reflective of the context (i.e. biofilm).
80 Integrative Metabolic Analysis Tool (iMAT) (27) is a method that has been developed to
81 incorporate expression data within a metabolic model. The iMAT algorithm uses a mixed
82 integer linear programming (MILP) problem to enrich pathways based on the expression data
83 while maintaining a steady flux distribution and the stoichiometric and thermodynamic
84 constraints. The iMAT model not only creates a phenotype specific model but post-
85 transcriptional regulation or inaccuracies in expression due to experimental limitations can be
86 predicted through this model as the surrounding fluxes would indicate the relative activity of
87 an enzyme in a pathway (27). By comparing the flux distributions of two context specific
88 models, changes in metabolic reactions between phenotypes can be predicted (28).

89 In this study, proteomic expression data was used to compare biofilm and planktonic
90 *B. pertussis* cells from a representative current circulating strain. Furthermore, the protein
91 expression data was incorporated into a GSMM to create context specific iMAT models to
92 elucidate key metabolic changes that may allow biofilm cells to persist in the host.

93 **Methods**

94 **Bacterial strains and biofilm growth**

95 A clinical *Bordetella pertussis* strain, L1423 isolated from the 2008-2012 Australian
96 epidemic with genotype *ptxP3/ptxA1/fim3A/prn2*, was used as a representative of the

97 predominant cluster I strains. The genome has been previously sequenced, and the strain has
98 been used in two separate infection studies in mice (29, 30). *B. pertussis* planktonic and
99 biofilm cells were grown using previously established methods and proteins were extracted
100 (31). Briefly, the *B. pertussis* strain was grown on Bordet-Gengou agar (BG, BD Scientific)
101 for 3-5 days at 37°C. A loopful of pure Bvg^+ colonies were suspended into Thalen-Ijssel
102 (THIJS) media (32) supplemented with 1% heptakis ((2,6-O-dimethyl) β-cyclodextrin) and
103 1% THIJS supplement and grown for 24 h shaking at 180 rpm at 37°C. For planktonic
104 growth, the OD_{600} of the starter culture was adjusted to 0.05 in 20 mL THIJS and incubated
105 for 12 h, shaking at 180 rpm. For biofilms, the OD_{600} was adjusted to 0.1 and 1 mL of this
106 adjusted culture was seeded into each well of a 24 well plate. The 24 well plate was incubated
107 statically for 5 h at 37°C for attachment of cells before the media was refreshed to remove
108 non-adherent cells (11). After 96 h of incubation, the wells were washed with PBS and then
109 the plate was water bath sonicated at 37 kHz for 2 min to detach cells. The planktonic and
110 biofilm cells were then probe sonicated and proteins extracted as described by Luu et al. (31).
111 Six biological replicates per condition were performed.

112 **Confocal laser scanning microscopy analysis**

113 To confirm biofilm maturity, confocal laser scanning microscopy (CLSM) was used.
114 This method was adapted from Cattelan et al. (33). The *B. pertussis* cells were grown on a
115 glass coverslip angled at 45° in the same method as described above. The biofilm was imaged
116 at 24, 48, 72 and 96 h. The biofilm was fixed with 4% paraformaldehyde and stained with
117 SYTO9 (Thermo Fisher Scientific) fluorescent dye. The coverslips were imaged on the
118 FluoView FV1200 inverted confocal microscope (Olympus Life Sciences) at the UNSW
119 Katharina Gaus Light Microscopy Facility (KG-LMF). Three biological replicates were
120 performed per time point and 3 field of views per replicate were randomly selected for z-
121 stack 3D imaging. The biomass was calculated using the COMSTAT2 ImageJ plugin (34).

122 **Protein preparation and LC-MS/MS**

123 The protein extracts (10 µg) were reduced with dithiothreitol, alkylated with
124 iodoacetamide and then digested with trypsin as described in Luu et al. (35). The peptides
125 were analysed on the LTQ-Orbitrap Velos mass spectrometer (Thermo Fisher Scientific) at
126 the UNSW Bioanalytical Mass Spectrometry Facility (BMSF) with the settings described in
127 Luu et al. (35). The output spectra were matched against a custom *B. pertussis* database on

128 the MaxQuant (v2.0.3.1) proteomics software with the following parameters: digestion mode
129 – specific, enzyme – Trypsin/P, max missed cleavages – 1, Label free quantification – LFQ,
130 Protein identification false discovery rate – 0.01 and min peptides per protein – 2. All other
131 parameters were set as the recommended default values. Student's *t*-test was calculated and a
132 false discovery rate (FDR) *q*-value multiple test correction was performed using the Storey-
133 Tibshirani method on R (v4.1.1) (36). Proteins were considered upregulated if the fold
134 change (FC) was > 1.2, $q < 0.05$ and downregulated if FC < 0.8, $q < 0.05$ based on previous
135 studies (31). Functional categories were assigned to proteins based on Bart et al. (37). The
136 mass spectrometry proteomics data have been deposited to the ProteomeXchange Consortium
137 via the PRIDE (38) partner repository with the dataset identifier PXD033664 and
138 10.6019/PXD033664.

139 **Integrated Metabolic Analysis Tool (iMAT) model generation**

140 The proteomic expression data was used to generate context specific metabolic
141 models for the planktonic and biofilm cells. The iMAT (39) method, available in the COBRA
142 Toolbox (v3.0) (40), was used. Processing was done in MATLAB (R2020a) using the IBM
143 CPLEX optimiser (v12.10.0). The iMAT algorithm extracts a simplified model based on the
144 trade-off between high expression and low expression reactions. The comprehensive,
145 manually curated *B. pertussis* metabolic model (iBP1870) generated by Branco dos Santos et
146 al. (23) was used as the base model. Subsystems from the *Escherichia coli* genome scale
147 metabolic model (iAF1260) were assigned to each of the reactions in the *B. pertussis* model
148 (41). The *E. coli* (iAF1260) model was used as a template for the original *B. pertussis* model
149 (iBP1870) and therefore, most of the subsystems are transferrable. The original *B. pertussis*
150 iBP1870 model had the tricarboxylic acid cycle partially dysfunctional (no flux from
151 oxaloacetate to α-ketoglutarate), as this model was based on previous studies which stated *B.*
152 *pertussis* has an incomplete TCA cycle (32). However, recent studies have shown that the
153 TCA cycle is fully functional and therefore the disabled pathways were activated before
154 generating the iMAT models (42). After refining the *B. pertussis* model, the biofilm and
155 planktonic proteins were assigned to the gene-protein-reaction (GPR) associations listed in
156 the *B. pertussis* model (iBP1870).

157 Label free quantification (LFQ) intensity values designated by the MaxQuant
158 software were used to estimate relative protein abundance. To increase confidence in the
159 imported data, only proteins identified in all six biological replicates per condition were

160 incorporated. Proteins were designated as uniquely identified if found in all 6 biological
161 replicates in one condition and none in the other. The expression data was defined as highly
162 (1), lowly (-1) or moderately (0) expressed based on the threshold of mean expression ± 0.5 x
163 STD of the proteins included in the model (39). After generating the planktonic and biofilm
164 context specific iMAT models, the reactions in the biofilm and planktonic models were
165 compared (Figure 1).

166 Additional infection specific models were generated with proteomic expression data
167 from two separate studies. The proteomic study by de Gouw et al. (11) compared *B. pertussis*
168 biofilm and planktonic (mid-log and stationery) cytosolic and membrane proteins. The
169 averaged expression values of the cytosolic and membrane fractionated proteins were
170 combined, and mid-log planktonic expression values were used to generate the models. The
171 study by Lamberti et al. (43) compared the proteomes of *B. pertussis* cells extracted from
172 within macrophages at 3 h and 48 h and planktonic cells. iMAT models were generated for
173 all three conditions. All models have been deposited to the BioModels database (44) in
174 SBML L3V1 format under the model identifier MODEL2205270001. Differences between
175 the growth conditions are listed in Supplementary Table S1.

176 **Flux Analysis**

177 A flux variability analysis (FVA) was performed on the models which provides
178 minimum and maximum permissible flux bounds for each reaction. Flux is recorded as a
179 millimolar concentration of metabolite per gram of dry cell weight per hour (mmol · g_{DCW}^{-1} ·
180 h^{-1}). The flux bounds in common reactions between the biofilm and planktonic models were
181 compared using the Jaccard index to calculate the similarity between the two models for each
182 reaction. The FVA is also important to determine which direction the reaction runs in the
183 model. Furthermore, to identify the most important reactions in each model, each reaction
184 was deleted in turn and an FVA calculation was performed to deem whether the model would
185 still be feasible without the reaction.

186 A flux balance analysis (FBA) was performed to identify changes in flux in reactions
187 shared by the planktonic and biofilm models. The FBA provides a single value for each
188 reaction based on a predefined metabolic goal so that the models may be compared. The FBA
189 method has been extensively developed to predict metabolic fluxes within metabolic models
190 (16). Typically, the objective function (*c*) of the linear optimisation equation is set as an

191 artificial biomass reaction as the metabolic goal of the organism. As generating biomass may
192 not be the metabolic objective of biofilm cells, an alternate method for defining the objective
193 function was used in this study. The objective function was defined based on proteomic
194 expression data as described in Montezano et al. (45). For all proteins that were identified
195 with GPR associations in the model, the intensities were normalised by the maximum
196 intensity value for each condition (planktonic and biofilm) and these values were input as *c*.
197 This leads the FBA to push flux towards the reactions which have higher protein expression
198 and considerably shrinks the solution space to increase prediction accuracy (45).

199 **Results**

200 **Key proteomic changes identified between biofilm and planktonic cells**

201 To identify changes that occur in biofilm conditions, label free quantification mass
202 spectrometry (LFQ-MS) was performed on biofilm and planktonic cells. Analysis was
203 performed on L1423, a clinical isolate representative of the current circulating *B. pertussis*
204 strains. Confocal microscopy confirmed biofilm formation and mature structure at 96 h
205 (Supplementary Figure S1). Furthermore, there was a polysaccharide biosynthesis protein,
206 WbpO (FC = 2.98, q = 1.17E-5) and a phosphoglucomutase enzyme, pgm (FC = 1.23, q =
207 0.041), that were seen to be upregulated in biofilm cells. These proteins have been previously
208 linked with *B. pertussis* biofilm reinforcing the biofilm phenotype achieved in this study (46).
209 There were 948 proteins identified in total, of which, 571 were proteins identified in all 6
210 biological replicates (Figure 2A). There were 478 proteins with significantly differential
211 expression ($q < 0.05$) between the two conditions. In biofilm cells, there were 242 proteins
212 downregulated and 236 proteins upregulated (Figure 2B).

213 There were many proteins related to virulence with altered expression identified in
214 this study (Table 1). BipA, an outer membrane protein associated with biofilm formation was
215 upregulated (11). Adenylate cyclase toxin (CyaA) and dermonecrotic toxin (Dnt) were also
216 upregulated in biofilm. There were 10 proteins from the Type III secretion system (T3SS)
217 that were downregulated in biofilm cells or uniquely identified in planktonic cells. One
218 protein (Bcr4) involved in the T3SS was upregulated in biofilm cells (47). Tracheal
219 colonisation factor (TcfA) and virulence associated gene 8 (Vag8) were downregulated in
220 biofilm cells while *Bordetella* resistance to killing (BrkA) protein was upregulated. Of the
221 ACV antigens, there was no change in expression for filamentous haemagglutinin (FhaB) but

222 the filamentous haemagglutinin outer membrane transporter protein (FhaC) was uniquely
223 identified in biofilm cells. The membrane bound pertussis toxin subunit 4 (PtxD) was also
224 uniquely identified in biofilm cells, however, pertussis toxin subunit 1 (PtxA) was
225 downregulated in biofilms. Furthermore, fimbriae protein (Fim2) was downregulated in
226 biofilm. Finally, pertactin (Prn) was strongly downregulated in biofilm (FC = 0.16, q =
227 2.42E-6). These changes demonstrate a strongly altered virulence profile in *B. pertussis*
228 biofilm cells compared to planktonic cells.

229 When the proteins were grouped into functional categories based on Bart et al. (37),
230 there was a significant increase in proteins in the categories of transport/binding and
231 miscellaneous proteins under biofilm conditions. There was also a downregulation of the
232 functional groups: ribosome constituents and cell processes (Figure 3).

233 **iMAT model generation**

234 For an in-depth analysis of the metabolic changes between biofilm and planktonic
235 cells, iMAT metabolic models were generated based on protein expression from both
236 conditions. Of the 571 proteins identified using mass spectrometry, 228 were annotated with
237 GPR associations in the *B. pertussis* (iBP1870) model (23). These are proteins which have
238 assigned reactions in the base model. The overlap between the identified proteins and the
239 reactions in the model constitutes 29.61% of the total GPR associations listed in the base
240 model. Context specific models were created using the iMAT algorithm implemented in the
241 COBRA Toolbox (40). The biofilm iMAT model consisted of 198 metabolites, 206 reactions
242 and 188 genes. The planktonic iMAT model had 213 metabolites, 219 reactions and 195
243 genes (Table 2). To identify changes between the planktonic and biofilm iMAT models, the
244 number of unique and common reactions between the two models were compared. There
245 were 168 reactions that were common between the two models, 51 reactions that were unique
246 to the planktonic model and 38 that were unique to the biofilm model (Figure 4A). The
247 reactions were grouped into subsystems and total number of reactions in each group were
248 similar between the two models (Figure 4B). It is notable however that there was a high
249 proportion of reactions that were unique to the individual models.

250 ***B. pertussis* biofilm cells complete the tricarboxylic acid cycle**

251 An FBA was performed to reveal changes in flux between reactions that were
252 common between the planktonic and biofilm models. A major difference was seen in the

253 tricarboxylic acid (TCA) cycle. The biofilm cells pushed flux to complete the TCA cycle
254 while the planktonic cells pushed flux towards the glyoxylate shunt (Figure 5). While there
255 was slightly higher levels of flux from oxaloacetate through to isocitrate in the planktonic
256 model (planktonic: 10.40 mmol · g_{DCW}^{-1} · h^{-1}, biofilm: 8.92 mmol · g_{DCW}^{-1} · h^{-1}), the
257 planktonic cells pushed all flux (11.31 mmol · g_{DCW}^{-1} · h^{-1}) into the glyoxylate shunt to
258 convert isocitrate to glyoxylate and succinate while comparatively, only a small flux (0.57
259 mmol · g_{DCW}^{-1} · h^{-1}) was pushed for the same reactions for biofilm cells. Instead, the flux
260 moved towards α-ketoglutarate (AKG) to succinyl-CoA and succinate to complete the TCA
261 cycle (Figure 5). The planktonic cells comparatively had no flux through these reactions.
262 Despite these changes, there was an increased level of flux from succinate to fumarate and
263 malate in the planktonic model which was fed from the glyoxylate shunt, branched chain
264 amino acid degradation and the arginine biosynthesis cycle. Finally, there was also increased
265 conversion of pyruvate to acetyl-CoA in the planktonic model which was then fed back into
266 the TCA cycle as citrate. Most of the acetyl-CoA synthesis/utilisation pathways were either
267 unique to the planktonic model or downregulated in the biofilm model. However, the biofilm
268 model had unique reactions to convert acetyl-CoA to polyhydroxybutyrate (PHB).

269 **Cardiolipin synthesis active in planktonic cells**

270 There were many reactions included in both models that were grouped into the
271 glycerophospholipid metabolism subsystem. Flux moves through the gluconeogenesis
272 pathway in both the models from pyruvate through to dihydroxyacetone phosphate and then
273 glycerol 3-phosphate (Figure 5). The pathways for most of the glycerophospholipids and fatty
274 acid synthesis were the same between the two models. However, the planktonic model had
275 pathways producing cardiolipin (tetradodecanoyl, n-C12:0) while the biofilm model lacked
276 these pathways. The production of cardiolipin is through the pathway of conversion of 1,2-
277 didodecanoyl-sn-glycero-3-cytidine 5'-diphosphate (CDP-DAG) to
278 phosphatidylglycerophosphate (didodecanoyl, n-C12:0) and therefore there is a higher level
279 of flux from the cytidine monophosphate (CMP) to cytidine triphosphate (CTP) in the
280 planktonic model. The models suggest that there would be a higher level of 1-dodecanoyl-*sn*-
281 glycerol 3-phosphate, 1-hexadec-9-enoyl-*sn*-glycerol 3-phosphate and glycerol 3-phosphate
282 in the periplasm of the biofilm cells. In the planktonic cells, there was a higher level of
283 cardiolipin, phosphatidylglycerol (didodecanoyl, n-C12:0), 2-dodecanoyl-*sn*-glycerol 3-
284 phosphate and 2-hexadec-9-enoyl-*sn*-glycerol 3-phosphate. The biofilm model uniquely

285 exported glycerol 3-phosphate into the extracellular space through these pathways while
286 planktonic model uniquely exported glycerol into the extracellular space (Figure 5).

287 **Arginine biosynthesis decreased in biofilm cells**

288 The metabolic models also revealed many altered amino acid metabolism pathways.
289 There was an equal number of reactions grouped into the arginine and proline metabolism
290 subsystem between the two models. However, the processes within the pathways were varied
291 as seen by the number of unique reactions within the subsystem (Figure 4B). Both models
292 feed into the arginine pathways through conversion of L-glutamate (GLU) to L-glutamine.
293 Subsequently, both models have reactions to produce carbamoyl phosphate (CBP). While the
294 planktonic model pushed the CBP into the arginine biosynthesis pathway, the biofilm model
295 had reactions to convert CBP through to orotate which was then exported out of the cell. The
296 planktonic cells complete the arginine biosynthesis cycle, exporting urea out of the cell as a
297 by-product. Furthermore, in the planktonic model, arginine succinate is converted to arginine
298 and fumarate which is fed back into the TCA cycle (Figure 5). When each of these reactions
299 were deleted in turn and tested for model feasibility, it led to infeasible models for the
300 planktonic model but were still feasible for the biofilm model (Supplementary Table S2).

301 Both models produced ornithine surrounding the arginine metabolism pathways. The
302 planktonic cells produced ornithine through the arginine biosynthesis pathway while the
303 biofilm cells synthesised ornithine through AKG to acetyl-ornithine and then to ornithine.
304 The fate of ornithine also differed greatly between the two models. When the FVA values
305 were compared, the smallest Jaccard index value (lowest similarity) between the models were
306 for the reactions acetylornithine transaminase (R_ACOTA) and glutamate N-acetyl
307 transferase (R_ORNTA). R_ACOTA is a reversible reaction of acetyl-ornithine and AKG to
308 N-acetyl-L-glutamate 5-semialdehyde and GLU. The FVA revealed that the biofilm model
309 only had capabilities to run this reaction in reverse. The opposite was seen for R_ORNTA, a
310 reversible reaction of acetyl-ornithine and GLU to ornithine and N-acetyl-L-glutamate. The
311 planktonic model ran this reaction in reverse. Overall, the ornithine in the planktonic model
312 was either utilised to produce acetate or pushed back through the arginine biosynthesis
313 pathway. The biofilm model pushed ornithine through the butanoate metabolism pathway
314 into the TCA cycle as succinate with the production of NADPH and NADH. This process
315 utilised GLU and produced AKG.

316 **Aspartate metabolism downregulated in biofilm cells**

317 Aspartate that was fed into the arginine biosynthesis pathway was decreased in
318 biofilm cells. Furthermore, when the reaction was deleted in the planktonic model, it led to an
319 infeasible model while the biofilm model remained feasible without the reaction. The flux in
320 the biofilm model pushed from aspartate through to threonine synthesis and CBP metabolism.
321 Threonine was then degraded through the branched chain amino acid (BCAA) degradation
322 pathway. Additionally, aspartate was uniquely converted with CBP to N-carbamoyl-L-
323 aspartate and ultimately into orotate as mentioned above for the biofilm model. The
324 planktonic model had flux flow from aspartate to homoserine, but rather than following
325 through to threonine, the homoserine was converted to O-acetyl-L-homoserine towards
326 acetate and L-cystathionine (Figure 5). L-cystathionine was then converted to L-cysteine and
327 2-oxobutanoate which was fed through the BCAA (specifically the isoleucine pathway)
328 degradation pathway that was upregulated in the planktonic model. The BCAA degradation
329 pathway leads to the production of acetyl-CoA, NADH, NADPH and $FADH_2$. There was
330 further production of these molecules through the valine degradation pathway in the
331 planktonic model. These pathways lead flux being moved back into the TCA cycle as
332 succinate and pyruvate through propanoate metabolism. Although the planktonic model
333 moved flux through the valine degradation pathway, the actual production of valine was
334 unique to the biofilm model. The valine was either exported out of the cell or converted to
335 AKG in the biofilm model.

336 Cysteine was transported into the cell at the same rate between the two models. Both
337 models source cysteine through diffusion, active ABC transport and the conversion of
338 glutathione and L-cysteinylglycine. The biofilm model pushed all flux of cysteine to L-
339 alanine while the planktonic model also has pathways to convert the cysteine through to
340 acetyl-CoA as mentioned above. The reactions to move L-alanine in and out of the periplasm
341 were unique to the biofilm model. The main source of L-alanine for the biofilm cells was
342 from the conversion of pyruvate and glutamine to L-alanine and AKG. The planktonic model
343 creates L-alanine through the conversion of β-alanine. This reaction also creates malonate-
344 semialdehyde and was strongly downregulated in the biofilm model. The L-alanine is
345 converted to D-alanine and then to GLU and pyruvate in both models.

346 **Biofilm cells have increased superoxide dismutase activity**

347 Both models converted ubiquinol to ubiquinone through cytochrome ubiquinol
348 oxidase. This reaction was downregulated in biofilm model. However, the biofilm model also
349 had an additional reaction that converted ubiquinol to ubiquinone with the by-product of
350 superoxide anions. The superoxide was converted to hydrogen peroxide and O_2 by
351 superoxide dismutase. The hydrogen peroxide was converted to H_2O by thioredoxin. The
352 other reactions involving ubiquinone were downregulated in biofilm cells including succinate
353 dehydrogenase and NADH dehydrogenase. However, ubiquinone was converted to ubiquinol
354 through the conversion S-dihydroorotate to orotate in a reaction unique to the biofilm cells.

355 **Comparison with other metabolic models**

356 We further used proteomics data from two previous *B. pertussis* studies to create
357 iMAT models and compare the reactions. The first study performed by de Gouw et al. (11)
358 grew *B. pertussis* biofilms on flat polypropylene beads in a glass column reactor for 72 h with
359 THIJS media refreshed every 24 h. The planktonic cells were extracted at both mid-
360 exponential phase at 17 h and stationary phase at 40 h. That study identified 729 – 825
361 proteins from the three different conditions with an overlap of 645 proteins (11). While the
362 biofilm iMAT model generated using that proteomic data had a higher number of reactions,
363 metabolites and genes to the planktonic iMAT model generated from that same data, the
364 overall values were comparable to the models of this study (Supplementary Table S1). The
365 second study that was compared was proteomic data from *B. pertussis* cells isolated from
366 within macrophages performed by Lamberti et al. (43). *B. pertussis* cells were extracted from
367 within macrophages at both 3 h and 48 h after infection in addition to a planktonic
368 counterpart grown in Roslyn Park Memorial Institute (RPMI)-1640-BSA 0.2% (*w/v*). A total
369 of 762 proteins were identified with 300 with differential expression between the conditions
370 (43). iMAT models were generated for these conditions and compared (Supplementary Table
371 S1). As with the additional models generated from the study by de Gouw et al. (11), the three
372 models generated by the Lamberti et al. (43) intracellular macrophage study yielded similar
373 numbers of reactions, metabolites and genes as with this present study

374 In line with our study, the de Gouw et al. (11) biofilm model completed the full TCA
375 cycle while the planktonic model pushed flux through the glyoxylate shunt. A similar trend
376 was identified for the models created from the Lamberti et al. (43) intracellular macrophage
377 study. The planktonic model showed the same preference for the glyoxylate shunt and the *B.*
378 *pertussis* cells extracted from the macrophages at 3 h had a similar flux through the TCA

379 cycle as the biofilm models, however, the 48 h model pushed flux through the glyoxylate
380 shunt.

381 Further similarities were identified between the intracellular macrophage and biofilm
382 models in NADH dehydrogenase, aspartate transaminase and CO_2 and O_2 exchange. All
383 intracellular macrophage and biofilm models had decreased flux in these reactions compared
384 to their planktonic counterpart. The NADH dehydrogenase reaction produces NAD+ from
385 NADH with the conversion of ubiquinone to ubiquinol. The aspartate transaminase reaction
386 (R_ASPTA - reversed) had decreased flux for all intracellular macrophage and biofilm
387 models. This reaction converted GLU and oxaloacetate to AKG and aspartate. The reaction
388 from aspartate to CBP and subsequent reactions to orotate were unique to the biofilm models
389 (Supplementary Table S2).

390

391 **Discussion**

392 Recent studies have shown that biofilms are an important aspect of *B. pertussis*
393 pathogenesis (33, 48, 49). Biofilm cells are more resilient against antimicrobials and
394 environmental stresses (12). While previous studies of *B. pertussis* biofilms have made
395 important discoveries related to growth and virulence, there has been less research focused on
396 biofilm metabolism. Biofilms are readily formed by *B. pertussis* and has been defined as an
397 integral part of its pathogenesis (7). Investigating the metabolic changes that occur within a
398 biofilm community may help understand the pathogenesis of *B. pertussis*. Therefore, this
399 study integrated proteomic expression data from a currently circulating epidemic strain into a
400 metabolic model of *B. pertussis* to identify major changes that occur in metabolism between
401 the biofilm and planktonic states. To our knowledge this is the first extensive study into
402 specific metabolic pathways within biofilms of *B. pertussis*. Although utilised metabolic
403 pathways differ from species to species, many of the changes in this study have been
404 identified and confirmed experimentally in other species reinforcing the strength of the
405 metabolic models. The major metabolic differences identified in this study relate to the TCA
406 cycle, amino acid metabolism and virulence.

407 The TCA cycle is the major central metabolic pathway for many aerobic organisms,
408 therefore it was surprising to find that there was altered flux for the TCA cycle. There was a
409 major shift in planktonic cells to utilise the glyoxylate shunt instead of completing the full

410 TCA cycle. The TCA reactions with increased flux in biofilms leads to the production of
411 NADH, NADPH and ATP. Variation in the glyoxylate shunt has been observed in the
412 biofilms of other species. When the glyoxylate shunt was disabled in *Pseudomonas*
413 *aeruginosa,* there was an increase in biofilm formation (50), which is reflected in this study.
414 It was suggested that the increased extracellular polymeric substances (EPS) produced when
415 the glyoxylate shunt was disabled could lead to higher survival in the microaerobic
416 conditions of the cystic fibrosis lung environment (50). Additionally, there was an increased
417 level of glyoxylate activity in *Candida albicans* cells dispersed from biofilm (51). It was
418 suggested that as the glyoxylate shunt is activated to increase nutrient versatility, it may be an
419 anticipatory reaction for low nutrient levels while searching for a new colonisation location
420 (51). The dispersed cells may reflect a planktonic lifestyle while established mature biofilm
421 cells may utilise the network of cells to share nutrients and hence have a decreased
422 requirement of the glyoxylate shunt. Targeting the TCA cycle has been suggested as a
423 potential therapeutic strategy against biofilms (52). Additional models that were created using
424 *B. pertussis* biofilm and planktonic proteomic expression data from de Gouw et al. (11) had
425 similar differences in the TCA cycle to our results (Supplementary Figure S2).

426 The glyoxylate shunt was also identified as important in intracellular macrophage survival.
427 Additional iMAT models created with *B. pertussis* proteomic expression data from Lamberti
428 et al. (43) showed that the glyoxylate shunt was inactive at 3 h inside macrophages but active
429 at 48 h (Supplementary Figure S2). This is reflective of previous studies that have shown that
430 inactivation of the glyoxylate shunt led to decreased macrophage intracellular survival (53,
431 54). The differences seen may be due to the need to scavenge nutrients in the hostile
432 environment and the time it takes for the bacteria to adapt to the new environment. The
433 additional models had limited altered pathways reflecting the other significant changes
434 identified in this study which may be due to the many differences between conditions
435 (Supplementary Table S1). However, it is noteworthy that the same pattern was seen with the
436 glyoxylate shunt in the biofilm and intracellular macrophage models compared to the
437 planktonic cells. This highlights the importance of the glyoxylate shunt as a key determinant
438 of virulence during *B. pertussis* infection.

439 Increased polyhydroxybutyrate (PHB) and superoxide dismutase activity may explain
440 the increased survivability of *B. pertussis* biofilm cells. Reactions regarding PHB synthesis
441 were identified as unique in the biofilm model and superoxide dismutase activity was

442 increased in the biofilm model. While most reactions surrounding acetyl-CoA were
443 downregulated in the biofilm model or unique in the planktonic model, one reaction that
444 involved the production of PHB was unique in biofilm. The PHB reactions led to an increase
445 in cytoplasmic PHB demand. It has been previously reported that cytoplasmic PHB
446 inclusions exist in *B. pertussis* cells. These inclusions are used as an energy reserve for when
447 cells are in harsh environments (32). As the PHB demand reactions are increased in the
448 biofilm cells, this may lead to increased cell survivability that has been observed in *B.*
449 *pertussis* biofilms (12). Furthermore, an increase in the superoxide dismutase activity is
450 protective as it leads to a decrease in superoxide which, as a free radical, may lead to cellular
451 damage (55). Put together, these two factors may be a reason for increased cell survivability
452 of *B. pertussis* biofilm cells and may lead to persistent infections.

453 Many pathways for glycerophospholipid metabolism were seen to be active in both
454 metabolic models. Lipid remodelling can occur when cells are exposed to harsh environments
455 or antimicrobials (56). The changes in the lipids have been linked to increased survivability
456 and persistence in pathogenic bacterial biofilms (57). The models in this study suggest that
457 there would be differing levels of certain glycerophospholipids in the periplasm between
458 planktonic and biofilm cells. Of particular interest is cardiolipin, identified as a unique lipid
459 synthesis pathway in the planktonic model. Previous studies have shown that cardiolipin
460 depletion led to decreased biofilm in *E. coli* (58). Cardiolipins have been identified in *B.*
461 *pertussis* previously however, studies have not remarked on biofilm cells (59). It is important
462 to note that the proteomic data captures enzymes that are active at a particular time point
463 rather than a measurement of lipids, therefore, the changes identified in these reactions
464 merely provide a snapshot of the time from which the proteins were harvested. The
465 planktonic cells may continuously synthesise cardiolipin while mature biofilm cells either
466 synthesise cardiolipin at an earlier stage of biofilm or have a lower requirement for
467 cardiolipin. To further investigate the changes in lipid composition, future lipidomic analysis
468 of biofilm cells would be necessary. Nevertheless, the evidence from the metabolic models in
469 this study suggest differing lipid composition in biofilm and planktonic *B. pertussis* cell
470 membranes. Another interesting change that was linked to the cardiolipin pathway was the
471 exportation of glycerol out of the cell. While the planktonic cells exported glycerol, the
472 biofilm cells exported glycerol 3-phosphate. The reason for this is unexplored and it would be
473 interesting to identify whether varying concentrations of glycerol 3-phosphate or glycerol
474 would have a regulatory role in *B. pertussis*.

475 Many regulatory processes are involved in *B. pertussis* biofilm formation (60). This
476 study identified multiple amino acid processing pathways that varied between biofilm and
477 planktonic cells. It has been reported previously that amino acids and their intermediates can
478 act as regulatory molecules (61-63). The planktonic cells showed increased arginine
479 biosynthesis and aspartate transaminase activity. It has been shown in other species that
480 arginine may increase biofilm formation although higher concentrations have an inhibitory
481 effect (62) and increase antibiotic killing (64). In addition, arginine may disrupt bacterial
482 coaggregation to prevent biofilm formation (65). Finally, the arginine biosynthesis process
483 leads to urea by-products which have been previously shown to disrupt the EPS matrix of
484 biofilms (66). The evidence in these studies combined with results from this present study
485 points to a tightly regulated arginine synthesis pathway which is partially fed by the aspartate
486 transaminase reaction. While the planktonic model pushed aspartate to the arginine
487 biosynthesis pathway, the biofilm cells pushed aspartate to the threonine degradation pathway
488 and towards the synthesis of N-carbamoyl-L-aspartate (through to orotate) leading to an
489 overall reduction of available arginine. The orotate was uniquely exported out of the biofilm
490 cells rather than processed for pyrimidine metabolism. Orotate therefore has the potential to
491 act as a signalling molecule for *B. pertussis* biofilm cells. The pathways regarding carbamoyl
492 phosphate synthesis which leads to orotate synthesis has been implicated in biofilm formation
493 in other species (67, 68). This orotate production pathway was specific to both the biofilm
494 model in this study and the biofilm model created from the data of de Gouw et al. (11),
495 reinforcing the possible importance of orotate export for *B. pertussis* biofilms.

496 While orotate metabolism may be specific to *B. pertussis* biofilm models, other
497 aspartate processing changes identified may be specific to broader infection environments.
498 Aspartate conversion from AKG (aspartate transaminase reaction) was seen to be a
499 downregulated pathway in all intracellular macrophage and biofilm metabolic models
500 compared to their planktonic counterparts. Aspartate feeds directly into the arginine
501 biosynthesis pathway as mentioned previously. Aspartate has been seen to inhibit biofilm
502 formation in multiple *Staphylococcus* species (69). Furthermore, the specific aspartate
503 transaminase reaction was downregulated in *Streptococcus pneumoniae* biofilms (70).
504 Interestingly, in *Mycobacterium tuberculosis* it was shown that the aspartate pathways are
505 important for intracellular survival in macrophages. It was suggested that intracellular *M.*
506 *tuberculosis* requires exogenous aspartate for intracellular survival and that it is a potential
507 target for novel therapeutics (71). The intracellular models generated in this study suggest

508 that exogenous aspartate scavenging is not as important for *B. pertussis* intracellular survival.
509 However, as it is important for the planktonic model, it may still provide a potential target to
510 prevent initial colonisation.

511 Finally, there was a change in the processing of alanine and valine between the
512 biofilm and planktonic models. The models suggest that β-alanine is important for planktonic
513 cells while L-alanine is more vital for biofilm cells. The biofilm model had unique reactions
514 transporting L-alanine into the periplasm. A recent study showed that alanine metabolism
515 activity displays a unique pattern based on spatial distribution of cells within a heterogenous
516 biofilm (72). The alanine metabolism changes identified in the present study may relate to a
517 particular layer of the biofilm. It would be interesting to see the specific active reactions
518 between the layers of biofilm. Proteomic analysis on layers of biofilm have previously been
519 performed using laser ablation sample transfer (LAST) and label free mass spectrometry (73).
520 A combination of LAST and the methods used in this study may be able to confirm the
521 changes in alanine metabolism. Furthermore, valine was uniquely exported out of the biofilm
522 model. This confirms what has been observed in other Gram-negative species that had
523 increased valine secretion in biofilm conditions (74). It was suggested that within the low
524 oxygen and reduced growth rate conditions of biofilms, there would be an excess of pyruvate
525 leading to an increase in valine and alanine biosynthesis (74). The discussed changes in
526 amino acid metabolism pathways are biofilm specific and therefore it is possible that the
527 secreted molecules could work as signalling molecules potentially triggering biofilm
528 formation.

529 Major expression differences were also identified for virulence factors. The Bvg
530 system has been shown to regulate most of the virulence factors in *B. pertussis* (75). In
531 addition, there are also secondary regulators that alter virulence factor expression in biofilm
532 cells (76). This study identified increased expression of the BvgA regulator and BvgS in
533 biofilms while the expression of BvgR was similar between the two conditions (Table 1).
534 Unexpectedly, there was a wide variability in protein expression within Bvg regulated
535 proteins. For example, Dnt and CyaA were upregulated while many proteins of the type III
536 secretion system (T3SS) and Prn were found to be downregulated in biofilm cells. To our
537 knowledge, this is the first report of a major downregulation of Prn in *B. pertussis* biofilm
538 cells. As one of the three ACV components, the change identified supports the hypothesis
539 that the planktonic based ACV may not protect as efficiently against cells in the biofilm

540 condition. To further reinforce this idea, the biofilm membrane derived protein that has been
541 suggested as a potential new addition to the vaccine, BipA was identified as upregulated in
542 biofilm cells in this study (11). Upregulation of BipA also underscores the importance of the
543 Bvg^i phase in the biofilm existence. There were also changes in both Bvg^+ and Bvg^- protein
544 regulation. Within both the upregulated and downregulated proteins, 13-15% of the proteins
545 were Bvg^+. Furthermore, there was a significantly higher proportion (14%) of proteins
546 upregulated in biofilms that were Bvg^- compared to the proportion (4%) of proteins
547 downregulated that were Bvg^- (Fishers exact test, $p = 0.0002$). The change in the expression
548 of these Bvg regulated proteins may be related to the 8 regulatory proteins with differential
549 expression in biofilm cells (Supplementary Table S2). The findings in this study point to
550 other major regulatory systems that affect the regulation of virulence proteins in biofilm
551 conditions.

552 The flux balance analysis identified reactions that have increased or decreased flux
553 within the models. There was a number of reactions with 0 $mmol \cdot g_{DCW}^{-1} \cdot h^{-1}$ flux. This is a
554 common issue that occurs with metabolic models (45). This is understandable as when the
555 objective function is set relative to the expression data, the mixed integer linear programming
556 calculation prioritises the reactions in the models with increased protein expression. This
557 leads to reactions that were not identified in the proteomic data recorded under the minimum
558 value, which is often 0 $mmol \cdot g_{DCW}^{-1} \cdot h^{-1}$ as revealed by the FVA flux bounds. Overall, the
559 0 $mmol \cdot g_{DCW}^{-1} \cdot h^{-1}$ flux reactions may lead to decreased accuracy in the mM
560 measurements of flux from the FBA but it does not invalidate the relative flux through
561 pathways when they are compared between the models. Additionally, the unique reactions
562 with 0 $mmol \cdot g_{DCW}^{-1} \cdot h^{-1}$ fluxes are still important for that model as designated by the
563 iMAT algorithm.

564 Traditional analysis of proteomic data involves grouping proteins into broad
565 functional categories to identify major changes, but it lacks the precision to examine specific
566 changes in metabolism. The incorporation of the proteomic data in the GSMM in this study
567 provided new insights into the metabolic pathways that were altered between biofilm and
568 planktonic cells. It is important to note that the biofilm cells were grown in an artificial media
569 designed to optimise *B. pertussis* growth. It would be interesting to see how growth in
570 different media such as media more representative of the respiratory environment or co-
571 culture with epithelial cells would affect the metabolic model (77). Additionally, it has been

572 shown that there is a wide range of heterogeneity of cells in a biofilm (78). This is not
573 surprising as cells within the biofilm would be exposed to varying levels of nutrient gradients
574 (79). As it is, the model in this study would have taken an average of overall expression and
575 there may have been important differences between the layers of biofilm that could improve
576 our understanding of the overall biofilm process. Additionally, it would be interesting to
577 create temporal metabolic models to identify the changes that occur throughout biofilm
578 development (80).

579 In conclusion, this study demonstrated major metabolic changes that occur during
580 biofilm conditions in *B. pertussis*. Many similar changes in biofilm pathways from other
581 species were also found in *B. pertussis,* reinforcing the utility of integrated expression data
582 into metabolic modelling. Notably, it was found that biofilm cells utilised the full TCA cycle
583 while planktonic cells pushed flux through the glyoxylate shunt. There was an increase in
584 PHB accumulation and superoxide dismutase activity which may lead to increased
585 persistence of biofilm cells. Major changes were identified in amino acid pathways including
586 exportation of valine out of biofilm cells which may have a role in cell-to-cell
587 communication. Finally, there were changes in virulence factor expression including an
588 increase in Dnt and CyaA and a strong downregulation of T3SS and Prn in biofilm cells.
589 Overall, the changes identified in this study helps lay the groundwork for further studies into
590 *B. pertussis* biofilms and their role in pathogenesis.

591

592 References

593 1. Galanis, E., A. S. King, P. Varughese, and S. A. Halperin. 2006. Changing epidemiology and
594 emerging risk groups for pertussis. *Can. Med. Assoc. J.* 174: 451-452.
595 2. de Melker, H. E., M. A. Conyn-van Spaendonck, H. C. Rümke, J. K. van Wijngaarden, F. R.
596 Mooi, and J. F. Schellekens. 1997. Pertussis in The Netherlands: an outbreak despite high
597 levels of immunization with whole-cell vaccine. *Emerg. Infect. Dis.* 3: 175-178.
598 3. Güriş, D., P. M. Strebel, B. Bardenheier, M. Brennan, R. Tachdjian, E. Finch, M. Wharton,
599 and J. R. Livengood. 1999. Changing epidemiology of pertussis in the United States:
600 increasing reported incidence among adolescents and adults, 1990-1996. *Clin. Infect. Dis.* 28:
601 1230-1237.
602 4. Campbell, P. T., J. M. McCaw, P. McIntyre, and J. McVernon. 2015. Defining long-term
603 drivers of pertussis resurgence, and optimal vaccine control strategies. *Vaccine* 33: 5794-
604 5800.
605 5. Octavia, S., R. P. Maharjan, V. Sintchenko, G. Stevenson, P. R. Reeves, G. L. Gilbert, and R.
606 Lan. 2011. Insight into Evolution of *Bordetella pertussis* from Comparative Genomic
607 Analysis: Evidence of Vaccine-Driven Selection. *Molecular Biology and Evolution* 28: 707-
608 715.
609 6. Mooi, F. R., N. A. Van Der Maas, and H. E. De Melker. 2014. Pertussis resurgence: waning
610 immunity and pathogen adaptation - two sides of the same coin. *Epidemiology and infection*
611 142: 685-694.
612 7. Conover, M. S., G. P. Sloan, C. F. Love, N. Sukumar, and R. Deora. 2010. The Bps
613 polysaccharide of *Bordetella pertussis* promotes colonization and biofilm formation in the
614 nose by functioning as an adhesin. *Mol. Microbiol.* 77: 1439-1455.
615 8. Goldsmith, C. S., J. Guarner, J. L. Montague, M. T. Eliason, P. W. Greer, S. R. Zaki, W.-J.
616 Shieh, C. D. Paddock, R. C. Holman, G. N. Sanden, K.-H. Wu, K. M. Tatti, A. A. Gal, J. D.
617 Cherry, and C. Langston. 2008. Pathology and Pathogenesis of Fatal *Bordetella pertussis*
618 Infection in Infants. *Clin. Infect. Dis.* 47: 328-338.
619 9. Soane, M. C., A. Jackson, D. Maskell, A. Allen, P. Keig, A. Dewar, G. Dougan, and R.
620 Wilson. 2000. Interaction of *Bordetella pertussis* with human respiratory mucosa *in vitro*.
621 *Respir. Med.* 94: 791-799.
622 10. Serra, D. O., M. S. Conover, L. Arnal, G. P. Sloan, M. E. Rodriguez, O. M. Yantorno, and R.
623 Deora. 2011. FHA-mediated cell-substrate and cell-cell adhesions are critical for *Bordetella*
624 *pertussis* biofilm formation on abiotic surfaces and in the mouse nose and the trachea. *PLoS*
625 *One* 6: e28811.
626 11. de Gouw, D., D. O. Serra, M. I. de Jonge, P. W. Hermans, H. J. Wessels, A. Zomer, O. M.
627 Yantorno, D. A. Diavatopoulos, and F. R. Mooi. 2014. The vaccine potential of *Bordetella*
628 *pertussis* biofilm-derived membrane proteins. *Emerg Microbes Infect* 3: e58.
629 12. Dorji, D., R. M. Graham, P. Richmond, A. Keil, and T. K. Mukkur. 2016. Biofilm forming
630 potential and antimicrobial susceptibility of newly emerged Western Australian *Bordetella*
631 *pertussis* clinical isolates. *Biofouling* 32: 1141-1152.
632 13. Carriquiriborde, F., P. Martin Aispuro, N. Ambrosis, E. Zurita, D. Bottero, M. E. Gaillard, C.
633 Castuma, E. Rudi, A. Lodeiro, and D. F. Hozbor. 2021. Pertussis Vaccine Candidate Based on
634 Outer Membrane Vesicles Derived From Biofilm Culture. *Front. Immunol.* 12: 730434.
635 14. Moon, K., R. P. Bonocora, D. D. Kim, Q. Chen, J. T. Wade, S. Stibitz, and D. M. Hinton.
636 2017. The BvgAS Regulon of *Bordetella pertussis*. *mBio* 8: e01526-01517.
637 15. Belcher, T., I. MacArthur, J. D. King, G. C. Langridge, M. Mayho, J. Parkhill, and A.
638 Preston. 2020. Fundamental differences in physiology of *Bordetella pertussis* dependent on
639 the two-component system Bvg revealed by gene essentiality studies. *Microb Genom* 6:
640 mgen000496.
641 16. Orth, J. D., I. Thiele, and B. Ø. Palsson. 2010. What is flux balance analysis? *Nat. Biotechnol.*
642 28: 245-248.
643 17. Fong, N. L., J. A. Lerman, I. Lam, B. O. Palsson, and P. Charusanti. 2013. Reconciling a
644 *Salmonella enterica* metabolic model with experimental data confirms that overexpression of

the glyoxylate shunt can rescue a lethal ppc deletion mutant. *FEMS Microbiol. Lett.* 342: 62-69.

18. Metz, Z. P., T. Ding, and D. J. Baumler. 2018. Using genome-scale metabolic models to compare serovars of the foodborne pathogen *Listeria monocytogenes*. *PLoS One* 13: e0198584.
19. Lobel, L., N. Sigal, I. Borovok, E. Ruppin, and A. A. Herskovits. 2012. Integrative Genomic Analysis Identifies Isoleucine and CodY as Regulators of *Listeria monocytogenes* Virulence. *PLoS Genet.* 8: e1002887.
20. Lee, D.-S., H. Burd, J. Liu, E. Almaas, O. Wiest, A.-L. Barabási, Z. N. Oltvai, and V. Kapatral. 2009. Comparative Genome-Scale Metabolic Reconstruction and Flux Balance Analysis of Multiple *Staphylococcus aureus* Genomes Identify Novel Antimicrobial Drug Targets. *J. Bacteriol.* 191: 4015-4024.
21. Rienksma, R. A., P. J. Schaap, V. A. P. Martins Dos Santos, and M. Suarez-Diez. 2018. Modeling the Metabolic State of *Mycobacterium tuberculosis* Upon Infection. *Frontiers in cellular and infection microbiology* 8: 264-264.
22. Gu, C., G. B. Kim, W. J. Kim, H. U. Kim, and S. Y. Lee. 2019. Current status and applications of genome-scale metabolic models. *Genome Biol.* 20: 121.
23. Branco Dos Santos, F., B. G. Olivier, J. Boele, V. Smessaert, P. De Rop, P. Krumpochova, G. W. Klau, M. Giera, P. Dehottay, B. Teusink, and P. Goffin. 2017. Probing the Genome-Scale Metabolic Landscape of *Bordetella pertussis*, the Causative Agent of Whooping Cough. *Applied and environmental microbiology* 83: e01528-01517.
24. Fyson, N., J. King, T. Belcher, A. Preston, and C. Colijn. 2017. A curated genome-scale metabolic model of *Bordetella pertussis* metabolism. *PLOS Computational Biology* 13: e1005639.
25. Gonyar, L. A., P. E. Gelbach, D. G. McDuffie, A. F. Koeppel, Q. Chen, G. Lee, L. M. Temple, S. Stibitz, E. L. Hewlett, J. A. Papin, F. H. Damron, and J. C. Eby. 2019. *In Vivo* Gene Essentiality and Metabolism in *Bordetella pertussis*. *mSphere* 4: e00694-00618.
26. Åkesson, M., J. Förster, and J. Nielsen. 2004. Integration of gene expression data into genome-scale metabolic models. *Metab. Eng.* 6: 285-293.
27. Zur, H., E. Ruppin, and T. Shlomi. 2010. iMAT: an integrative metabolic analysis tool. *Bioinformatics* 26: 3140-3142.
28. Stempler, S., K. Yizhak, and E. Ruppin. 2014. Integrating Transcriptomics with Metabolic Modeling Predicts Biomarkers and Drug Targets for Alzheimer's Disease. *PLoS One* 9: e105383.
29. Safarchi, A., S. Octavia, L. D. W. Luu, C. Y. Tay, V. Sintchenko, N. Wood, H. Marshall, P. McIntyre, and R. Lan. 2016. Better colonisation of newly emerged *Bordetella pertussis* in the co-infection mouse model study. *Vaccine* 34: 3967-3971.
30. Safarchi, A., S. Octavia, L. D. W. Luu, C. Y. Tay, V. Sintchenko, N. Wood, H. Marshall, P. McIntyre, and R. Lan. 2015. Pertactin negative *Bordetella pertussis* demonstrates higher fitness under vaccine selection pressure in a mixed infection model. *Vaccine* 33: 6277-6281.
31. Luu, L. D. W., S. Octavia, L. Zhong, M. J. Raftery, V. Sintchenko, and R. Lan. 2018. Proteomic Adaptation of Australian Epidemic *Bordetella pertussis*. *Proteomics* 18: 1700237.
32. Thalen, M., I. J. van den, W. Jiskoot, B. Zomer, P. Roholl, C. de Gooijer, C. Beuvery, and J. Tramper. 1999. Rational medium design for *Bordetella pertussis*: basic metabolism. *J. Biotechnol.* 75: 147-159.
33. Cattelan, N., O. M. Yantorno, and R. Deora. 2018. Structural Analysis of *Bordetella pertussis* Biofilms by Confocal Laser Scanning Microscopy. *Bio Protocol* 8: e2953.
34. Heydorn, A., A. T. Nielsen, M. Hentzer, C. Sternberg, M. Givskov, B. K. Ersboll, and S. Molin. 2000. Quantification of biofilm structures by the novel computer program COMSTAT. *Microbiology* 146 (Pt 10): 2395-2407.
35. Luu, L. D. W., S. Octavia, L. Zhong, M. Raftery, V. Sintchenko, and R. Lan. 2017. Characterisation of the *Bordetella pertussis* secretome under different media. *J. Proteomics* 158: 43-51.

36. Storey, J. D., and R. Tibshirani. 2003. Statistical significance for genomewide studies. *Proceedings of the National Academy of Sciences* 100: 9440-9445.
37. Bart, M. J., S. R. Harris, A. Advani, Y. Arakawa, D. Bottero, V. Bouchez, P. K. Cassiday, C.-S. Chiang, T. Dalby, N. K. Fry, M. E. Gaillard, M. van Gent, N. Guiso, H. O. Hallander, E. T. Harvill, Q. He, H. G. J. van der Heide, K. Heuvelman, D. F. Hozbor, K. Kamachi, G. I. Karataev, R. Lan, A. Lutyńska, R. P. Maharjan, J. Mertsola, T. Miyamura, S. Octavia, A. Preston, M. A. Quail, V. Sintchenko, P. Stefanelli, M. L. Tondella, R. S. W. Tsang, Y. Xu, S.-M. Yao, S. Zhang, J. Parkhill, and F. R. Mooi. 2014. Global Population Structure and Evolution of *Bordetella pertussis* and Their Relationship with Vaccination. *mBio* 5: e01074-01014.
38. Perez-Riverol, Y., J. Bai, C. Bandla, D. García-Seisdedos, S. Hewapathirana, S. Kamatchinathan, D. J. Kundu, A. Prakash, A. Frericks-Zipper, M. Eisenacher, M. Walzer, S. Wang, A. Brazma, and J. A. Vizcaíno. 2022. The PRIDE database resources in 2022: a hub for mass spectrometry-based proteomics evidences. *Nucleic Acids Res.* 50: D543-d552.
39. Zur, H., E. Ruppin, and T. Shlomi. 2010. iMAT: an integrative metabolic analysis tool. *Bioinformatics* 26: 3140-3142.
40. Heirendt, L., S. Arreckx, T. Pfau, S. N. Mendoza, A. Richelle, A. Heinken, H. S. Haraldsdóttir, J. Wachowiak, S. M. Keating, V. Vlasov, S. Magnusdóttir, C. Y. Ng, G. Preciat, A. Žagare, S. H. J. Chan, M. K. Aurich, C. M. Clancy, J. Modamio, J. T. Sauls, A. Noronha, A. Bordbar, B. Cousins, D. C. El Assal, L. V. Valcarcel, I. Apaolaza, S. Ghaderi, M. Ahookhosh, M. Ben Guebila, A. Kostromins, N. Sompairac, H. M. Le, D. Ma, Y. Sun, L. Wang, J. T. Yurkovich, M. A. P. Oliveira, P. T. Vuong, L. P. El Assal, I. Kuperstein, A. Zinovyev, H. S. Hinton, W. A. Bryant, F. J. Aragón Artacho, F. J. Planes, E. Stalidzans, A. Maass, S. Vempala, M. Hucka, M. A. Saunders, C. D. Maranas, N. E. Lewis, T. Sauter, B. Ø. Palsson, I. Thiele, and R. M. T. Fleming. 2019. Creation and analysis of biochemical constraint-based models using the COBRA Toolbox v.3.0. *Nat. Protoc.* 14: 639-702.
41. Feist, A. M., C. S. Henry, J. L. Reed, M. Krummenacker, A. R. Joyce, P. D. Karp, L. J. Broadbelt, V. Hatzimanikatis, and B. Ø. Palsson. 2007. A genome-scale metabolic reconstruction for *Escherichia coli* K-12 MG1655 that accounts for 1260 ORFs and thermodynamic information. *Mol. Syst. Biol.* 3: 121-121.
42. Izac, M., D. Garnier, D. Speck, and N. D. Lindley. 2015. A Functional Tricarboxylic Acid Cycle Operates during Growth of *Bordetella pertussis* on Amino Acid Mixtures as Sole Carbon Substrates. *PLoS One* 10: e0145251.
43. Lamberti, Y., J. H. Cafiero, K. Surmann, H. Valdez, J. Holubova, B. Večerek, P. Sebo, F. Schmidt, U. Völker, and M. E. Rodriguez. 2016. Proteome analysis of *Bordetella pertussis* isolated from human macrophages. *J. Proteomics* 136: 55-67.
44. Malik-Sheriff, R. S., M. Glont, T. V. N. Nguyen, K. Tiwari, M. G. Roberts, A. Xavier, M. T. Vu, J. Men, M. Maire, S. Kananathan, E. L. Fairbanks, J. P. Meyer, C. Arankalle, T. M. Varusai, V. Knight-Schrijver, L. Li, C. Dueñas-Roca, G. Dass, S. M. Keating, Y. M. Park, N. Buso, N. Rodriguez, M. Hucka, and H. Hermjakob. 2019. BioModels—15 years of sharing computational models in life science. *Nucleic Acids Res.* 48: D407-D415.
45. Montezano, D., L. Meek, R. Gupta, L. E. Bermudez, and J. C. M. Bermudez. 2015. Flux Balance Analysis with Objective Function Defined by Proteomics Data—Metabolism of *Mycobacterium tuberculosis* Exposed to Mefloquine. *PLoS One* 10: e0134014.
46. Serra, D. O., G. Lucking, F. Weiland, S. Schulz, A. Gorg, O. M. Yantorno, and M. Ehling-Schulz. 2008. Proteome approaches combined with Fourier transform infrared spectroscopy revealed a distinctive biofilm physiology in *Bordetella pertussis*. *Proteomics* 8: 4995-5010.
47. Goto, M., A. Abe, T. Hanawa, and A. Kuwae. 2021. Bcr4 is a Chaperone for the Inner Rod Protein in the *Bordetella* Type III Secretion System. *bioRxiv*: 2021.2009.2028.462275.
48. Arnal, L., T. Grunert, N. Cattelan, D. de Gouw, M. I. Villalba, D. O. Serra, F. R. Mooi, M. Ehling-Schulz, and O. M. Yantorno. 2015. *Bordetella pertussis* Isolates from Argentinean Whooping Cough Patients Display Enhanced Biofilm Formation Capacity Compared to Tohama I Reference Strain. *Front. Microbiol.* 6: 1352.

751 49. Bosch, A., D. Serra, C. Prieto, J. Schmitt, D. Naumann, and O. Yantorno. 2005.
752 Characterization of *Bordetella pertussis* growing as biofilm by chemical analysis and FT-IR
753 spectroscopy. *Applied Microbiology and Biotechnology* 71: 736.
754 50. Ahn, S., J. Jung, I.-A. Jang, E. L. Madsen, and W. Park. 2016. Role of Glyoxylate Shunt in
755 Oxidative Stress Response. *Journal of Biological Chemistry* 291: 11928-11938.
756 51. Uppuluri, P., M. Acosta Zaldívar, M. Z. Anderson, M. J. Dunn, J. Berman, J. L. Lopez Ribot,
757 and J. R. Köhler. 2018. *Candida albicans* Dispersed Cells Are Developmentally Distinct from
758 Biofilm and Planktonic Cells. *mBio* 9: e01338-01318.
759 52. Yahya, M., U. Hamid, M. Norfatimah, and R. Kambol. 2014. *In silico* analysis of essential
760 tricarboxylic acid cycle enzymes from biofilm-forming bacteria. *Trends in Bioinformatics* 7:
761 19-26.
762 53. Rivera, I., B. Linz, K. K. Dewan, L. Ma, C. A. Rice, D. E. Kyle, and E. T. Harvill. 2019.
763 Conservation of Ancient Genetic Pathways for Intracellular Persistence Among Animal
764 Pathogenic Bordetellae. *Front. Microbiol.* 10: 2839.
765 54. McKinney, J. D., K. Höner zu Bentrup, E. J. Muñoz-Elías, A. Miczak, B. Chen, W. T. Chan,
766 D. Swenson, J. C. Sacchettini, W. R. Jacobs, Jr., and D. G. Russell. 2000. Persistence of
767 *Mycobacterium tuberculosis* in macrophages and mice requires the glyoxylate shunt enzyme
768 isocitrate lyase. *Nature* 406: 735-738.
769 55. Suo, Y., Y. Huang, Y. Liu, C. Shi, and X. Shi. 2012. The expression of superoxide dismutase
770 (SOD) and a putative ABC transporter permease is inversely correlated during biofilm
771 formation in *Listeria monocytogenes* 4b G. *PLoS One* 7: e48467-e48467.
772 56. Seydlova, G., J. Beranova, I. Bibova, A. Dienstbier, J. Drzmisek, J. Masin, R. Fiser, I.
773 Konopasek, and B. Vecerek. 2017. The extent of the temperature-induced membrane
774 remodeling in two closely related *Bordetella* species reflects their adaptation to diverse
775 environmental niches. *J. Biol. Chem.* 292: 8048-8058.
776 57. Dubois-Brissonnet, F., E. Trotier, and R. Briandet. 2016. The Biofilm Lifestyle Involves an
777 Increase in Bacterial Membrane Saturated Fatty Acids. *Front. Microbiol.* 7: 1673.
778 58. Nepper, J. F., Y. C. Lin, and D. B. Weibel. 2019. Rcs Phosphorelay Activation in Cardiolipin-
779 Deficient *Escherichia coli* Reduces Biofilm Formation. *J. Bacteriol.* 201: e00804-00818.
780 59. Kawai, Y., and A. Moribayashi. 1982. Characteristic lipids of *Bordetella pertussis*: simple
781 fatty acid composition, hydroxy fatty acids, and an ornithine-containing lipid. *J. Bacteriol.*
782 151: 996-1005.
783 60. Cattelan, N., P. Dubey, L. Arnal, O. M. Yantorno, and R. Deora. 2016. *Bordetella* biofilms: a
784 lifestyle leading to persistent infections. *Pathogens and Disease* 74: ftv108.
785 61. Cava, F., H. Lam, M. A. de Pedro, and M. K. Waldor. 2011. Emerging knowledge of
786 regulatory roles of D-amino acids in bacteria. *Cell Mol Life Sci* 68: 817-831.
787 62. Goh, S.-N., A. Fernandez, S.-Z. Ang, W.-Y. Lau, D.-L. Ng, and E. S. G. Cheah. 2013. Effects
788 of Different Amino Acids on Biofilm Growth, Swimming Motility and Twitching Motility in
789 *Escherichia coli* BL21. *Journal of Biology and Life Science* 4: 13.
790 63. Aliashkevich, A., L. Alvarez, and F. Cava. 2018. New Insights Into the Mechanisms and
791 Biological Roles of D-Amino Acids in Complex Eco-Systems. *Front. Microbiol.* 9: 683.
792 64. Borriello, G., L. Richards, G. D. Ehrlich, and P. S. Stewart. 2006. Arginine or Nitrate
793 Enhances Antibiotic Susceptibility of *Pseudomonas aeruginosa* in Biofilms. *Antimicrob.*
794 *Agents Chemother.* 50: 382-384.
795 65. Kolderman, E., D. Bettampadi, D. Samarian, S. E. Dowd, B. Foxman, N. S. Jakubovics, and
796 A. H. Rickard. 2015. L-Arginine Destabilizes Oral Multi-Species Biofilm Communities
797 Developed in Human Saliva. *PLoS One* 10: e0121835.
798 66. Brindle, E. R., D. A. Miller, and P. S. Stewart. 2011. Hydrodynamic deformation and removal
799 of *Staphylococcus epidermidis* biofilms treated with urea, chlorhexidine, iron chloride, or
800 DispersinB. *Biotechnology and bioengineering* 108: 2968-2977.
801 67. Zhuo, T., W. Rou, X. Song, J. Guo, X. Fan, G. G. Kamau, and H. Zou. 2015. Molecular study
802 on the *carAB* operon reveals that *carB* gene is required for swimming and biofilm formation
803 in *Xanthomonas citri* subsp. *citri*. *BMC Microbiol.* 15: 225-225.

68. Pisithkul, T., J. W. Schroeder, E. A. Trujillo, P. Yeesin, D. M. Stevenson, T. Chaiamarit, J. J. Coon, J. D. Wang, D. Amador-Noguez, J.-M. Ghigo, and E. P. Greenberg. 2019. Metabolic Remodeling during Biofilm Development of *Bacillus subtilis*. *mBio* 10: e00623-00619.
69. Yang, H., M. Wang, J. Yu, and H. Wei. 2015. Aspartate inhibits *Staphylococcus aureus* biofilm formation. *FEMS Microbiol. Lett.* 362: fnv025.
70. Allan, R. N., P. Skipp, J. Jefferies, S. C. Clarke, S. N. Faust, L. Hall-Stoodley, and J. Webb. 2014. Pronounced metabolic changes in adaptation to biofilm growth by *Streptococcus pneumoniae*. *PLoS One* 9: e107015.
71. Hasenoehrl, E. J., D. Rae Sajorda, L. Berney-Meyer, S. Johnson, J. M. Tufariello, T. Fuhrer, G. M. Cook, W. R. Jacobs, and M. Berney. 2019. Derailing the aspartate pathway of *Mycobacterium tuberculosis* to eradicate persistent infection. *Nature Communications* 10: 4215.
72. Díaz-Pascual, F., M. Lempp, K. Nosho, H. Jeckel, J. K. Jo, K. Neuhaus, R. Hartmann, E. Jelli, M. F. Hansen, A. Price-Whelan, L. E. P. Dietrich, H. Link, and K. Drescher. 2021. Spatial alanine metabolism determines local growth dynamics of *Escherichia coli* colonies. *eLife* 10: e70794.
73. Pulukkody, A. C., Y. P. Yung, F. Donnarumma, K. K. Murray, R. P. Carlson, and L. Hanley. 2021. Spatially resolved analysis of *Pseudomonas aeruginosa* biofilm proteomes measured by laser ablation sample transfer. *PLoS One* 16: e0250911.
74. Valle, J., S. Da Re, S. Schmid, D. Skurnik, R. D'Ari, and J. M. Ghigo. 2008. The amino acid valine is secreted in continuous-flow bacterial biofilms. *J. Bacteriol.* 190: 264-274.
75. Cotter, P. A., and A. M. Jones. 2003. Phosphorelay control of virulence gene expression in *Bordetella*. *Trends Microbiol.* 11: 367-373.
76. Bone, M. A., A. J. Wilk, A. I. Perault, S. A. Marlatt, E. V. Scheller, R. Anthouard, Q. Chen, S. Stibitz, P. A. Cotter, and S. M. Julio. 2017. Bordetella PlrSR regulatory system controls BvgAS activity and virulence in the lower respiratory tract. *Proceedings of the National Academy of Sciences* 114: E1519-E1527.
77. Palmer, K. L., L. M. Aye, and M. Whiteley. 2007. Nutritional cues control *Pseudomonas aeruginosa* multicellular behavior in cystic fibrosis sputum. *J. Bacteriol.* 189: 8079-8087.
78. Williamson, K. S., L. A. Richards, A. C. Perez-Osorio, B. Pitts, K. McInnerney, P. S. Stewart, and M. J. Franklin. 2012. Heterogeneity in *Pseudomonas aeruginosa* Biofilms Includes Expression of Ribosome Hibernation Factors in the Antibiotic-Tolerant Subpopulation and Hypoxia-Induced Stress Response in the Metabolically Active Population. *J. Bacteriol.* 194: 2062-2073.
79. Salgar-Chaparro, S. J., K. Lepkova, T. Pojtanabuntoeng, A. Darwin, L. L. Machuca, and A. J. M. Stams. 2020. Nutrient Level Determines Biofilm Characteristics and Subsequent Impact on Microbial Corrosion and Biocide Effectiveness. *Applied and environmental microbiology* 86: e02885-02819.
80. Siriwach, R., F. Matsuda, K. Yano, and M. Y. Hirai. 2020. Drought Stress Responses in Context-Specific Genome-Scale Metabolic Models of *Arabidopsis thaliana*. *Metabolites* 10: 159.

847 **Tables**

848 **Table 1** Virulence proteins differentially expressed or uniquely identified between planktonic
849 and biofilm cells

Locus	Gene	Product	Fold change (Biofilm/Planktonic)	*t*-Test ($p \leq 0.05$)	*q*-Value ($q \leq 0.05$)
BP0499	*btcA*	Type III secretion chaperone	0.594	0.002	0.0005
BP0500	*bteA*	Type III secretion toxin, effector	0.131	9.02E-08	2.52E-07
BP0760	*cyaA*	Bifunctional hemolysin-adenylate cyclase	1.530	0.042	0.008
BP1054	*prn*	Pertactin autotransporter	0.163	2.19E-06	2.42E-06
BP1112	*bipA*	Outer membrane ligand binding protein	2.073	3.65E-06	3.4E-06
BP1119	*fim2*	Serotype 2 fimbrial subunit	0.590	0.002	0.0006
BP1201	*tcfA*	Tracheal colonisation factor	0.070	2.94E-05	1.64E-05
BP1251	-	Putative toxin	Planktonic unique		
BP1877	*bvgS*	Virulence sensor protein BvgS	1.876	5.63E-05	2.77E-05
BP1878	*bvgA*	Virulence factors transcription regulator BvgA	3.101	1.69E-06	2.02E-06
BP1884	*fhaC*	Filamentous hemagglutinin transporter protein FhaC	Biofilm unique		
BP2233	*bspR*	Type III secretion chaperone	0.430	1.66E-06	2.02E-06
BP2236	*bscW*	Type III secretion chaperone	Planktonic unique		
BP2250	*bcr4*	Type III secretion protein	1.533	0.027	0.005
BP2251	*bcrH2*	Type III secretion chaperone	0.324	1.38E-08	8.98E-08
BP2253	*bopD*	Type III secretion system outer protein D	0.116	7.61E-10	1.49E-08
BP2255	*btc22*	Type III secretion protein chaperone	Planktonic unique		
BP2256	*bsp22*	Type III secretion tip protein	Planktonic unique		
BP2257	*bopN*	Type III secretion outer protein N, effector	Planktonic unique		
BP2263	*bscE*	Type III secretion protein	0.282	3.24E-08	1.73E-07
BP2315	*vag8*	Autotransporter	0.429	1.39E-05	9.03E-06
BP3439	*dnt*	Dermonecrotic toxin	1.429	0.135	0.022
BP3494	*brkA*	BrkA autotransporter	1.218	0.139	0.023
BP3654	*cyaY*	Iron-sulfur cluster assembly protein CyaY	0.618	0.188	0.030
BP3783	*ptxA*	Pertussis toxin subunit 1	0.299	1.37E-06	1.75E-06
BP3785	*ptxD*	Pertussis toxin subunit 4	Biofilm unique		

850

851

852 **Table 2** Number of metabolites, reactions and genes in the iMAT context specific models for
853 *B. pertussis* biofilm and planktonic cells.

	Biofilm	**Planktonic**
High expression (+1)	36	36
Moderate expression (0)	117	86
Low expression (-1)	65	78
Total proteins incorporated	218	200
iMAT models		
Metabolites	198	213
Reactions	206	219
Genes	188	195

854

855 **Figures**

856 **Figure 1 Experimental design for iMAT model generation**. Proteins were extracted from
857 planktonic and biofilm *B. pertussis* cells. The expression values were then used to generate
858 context specific metabolic models based on the extensively curated iBP1870 *B. pertussis*
859 model (23). Flux balance analysis was run on the models and the altered reactions compared
860 between the planktonic and biofilm models.

861 **Figure 2 Volcano plot of total protein expression changes between biofilm and**
862 **planktonic cells. A** Expression profile of all proteins identified through the LC-MS/MS
863 analysis of planktonic and biofilm *B. pertussis* cells. Proteins are plotted on a volcano plot
864 displaying the $\log_2$(*q*-value) on the y-axis and $\log_2$(fold change [biofilm/planktonic]) on the
865 x-axis. The dashed vertical grey lines mark a fold change of 0.8 and 1.2 and the horizontal
866 line marks the threshold of *q*-value = 0.05. Highlighted in red are the proteins that were
867 identified in all 6 biological replicates that were incorporated into the iMAT models. **B**
868 Expression profile of the subset of proteins incorporated into the iMAT model. Red markers
869 are proteins that were designated significantly differentially downregulated and the blue
870 markers are proteins that were significantly upregulated in biofilm cells. The dashed vertical

871 grey lines mark a fold change of 0.8 and 1.2 and the horizontal line marks the threshold of *q*-
872 value = 0.05.

873 **Figure 3 Proteins up and downregulated in *B. pertussis* biofilm cells compared to**
874 **planktonic cells identified using LC-MS/MS.** Proteins significantly up and downregulated
875 in biofilm cells were categorised in functional categories based on Bart et al. (37). Red and
876 blue bars represent the total number of proteins within the functional category significantly
877 up or downregulated, respectively. Asterisk (*) denotes functional categories significantly up
878 or downregulated based on Fisher's exact test with Benjamini-Hochberg multiple test
879 correction.

880 **Figure 4 Comparison of reactions of *B. pertussis* planktonic and biofilm iMAT models.**
881 **A** Venn diagram highlighting common and unique reactions between planktonic and biofilm
882 iMAT models generated by incorporating proteomic expression data. **B** Planktonic and
883 biofilm model reactions grouped into subsystems based on the *Escherichia coli* iAF1260
884 metabolic model. Unique reactions identified in one model but not the other are highlighted
885 in different colours on the graph.

886 **Figure 5 Summarised pathways with major changes between planktonic and biofilm**
887 **iMAT models.** Major changed core metabolic reactions were summarised and represented in
888 a model. The model includes the reactions that were unique in either model as well as
889 reactions with altered flux. Ac, Acetate; Ac-CoA, Acetyl-CoA; Akg, α-ketoglutarate; Ala,
890 Alanine; Arg, Arginine; Asp, Aspartate; BCAA, Branched chain amino acid degradation;
891 Cbp, Carbamoyl phosphate; Cgly, Cysteinylglycine; Cit, Citrate; CO_2, Carbon dioxide; Cys,
892 Cysteine; Fum, Fumarate; Gln, Glutamine; Glu, Glutamate; Glx, Glyoxylate; Gly, Glycine;
893 Gly3p, Glycine 3-phosphate; Glyc, Glycine; GNG, Gluconeogenesis; GPL,
894 Glycerophospholipid metabolism; Gthrd, Glutathione; Hom, Homoserine; Lac, Lactate; Mal,
895 Malate; O_2, Oxygen; OAA, Oxaloacetate; Orn, Ornithine; Orot, Orotate; Phb,
896 Polyhydroxybutyrate; Prop, Propanoate metabolism; Ptrc, Putrescine; Pyr, Pyruvate; SO_2,
897 Sulfur dioxide; Suc, Succinate; TCA, Tricarboxcylic acid cycle; Thr, Threonine; Val, Valine.
898

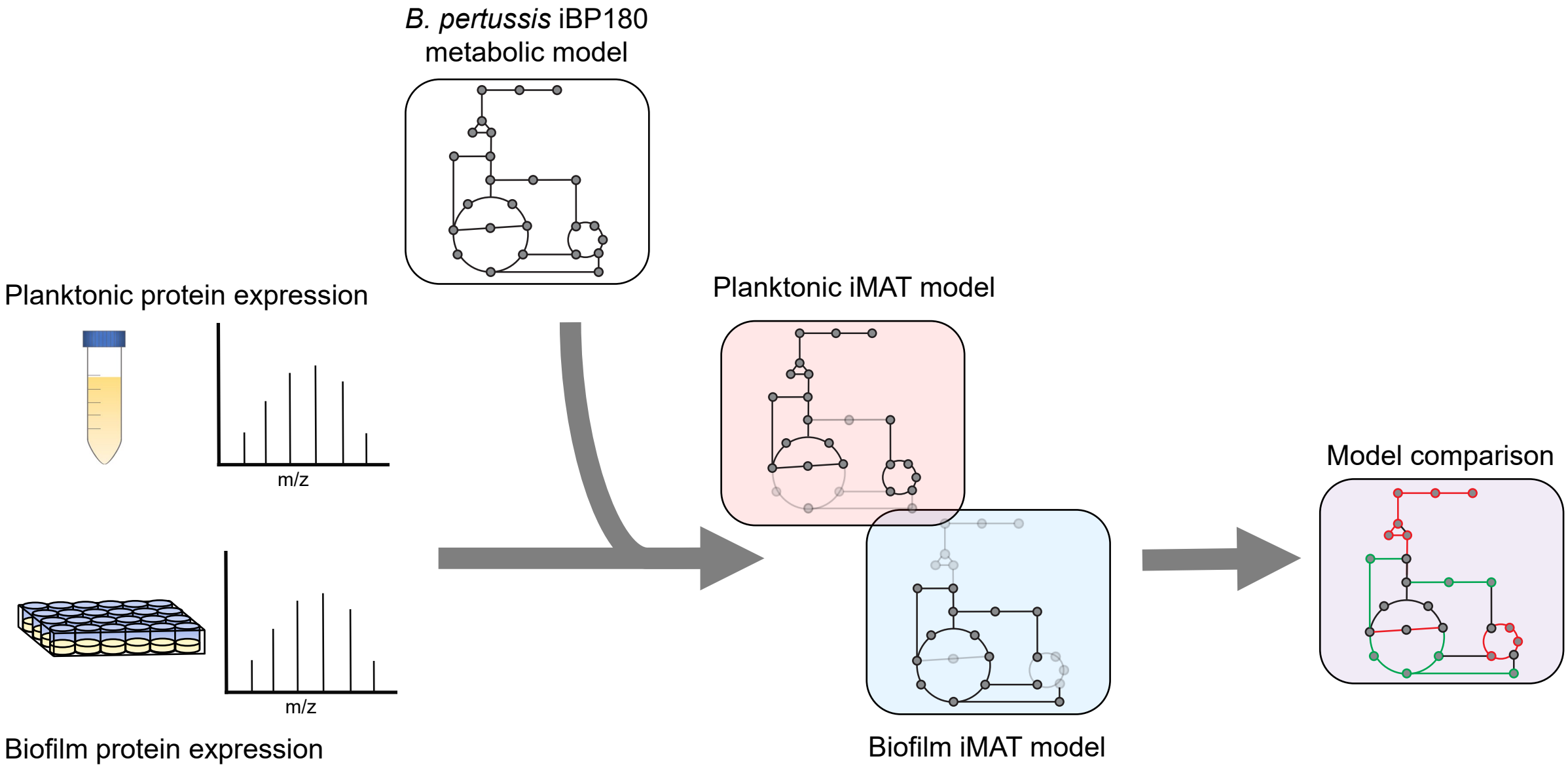
B. pertussis iBP180
metabolic model
Planktonic protein expression
m/z
m/z
Biofilm protein expression
Planktonic iMAT model
Biofilm iMAT model
Model comparison

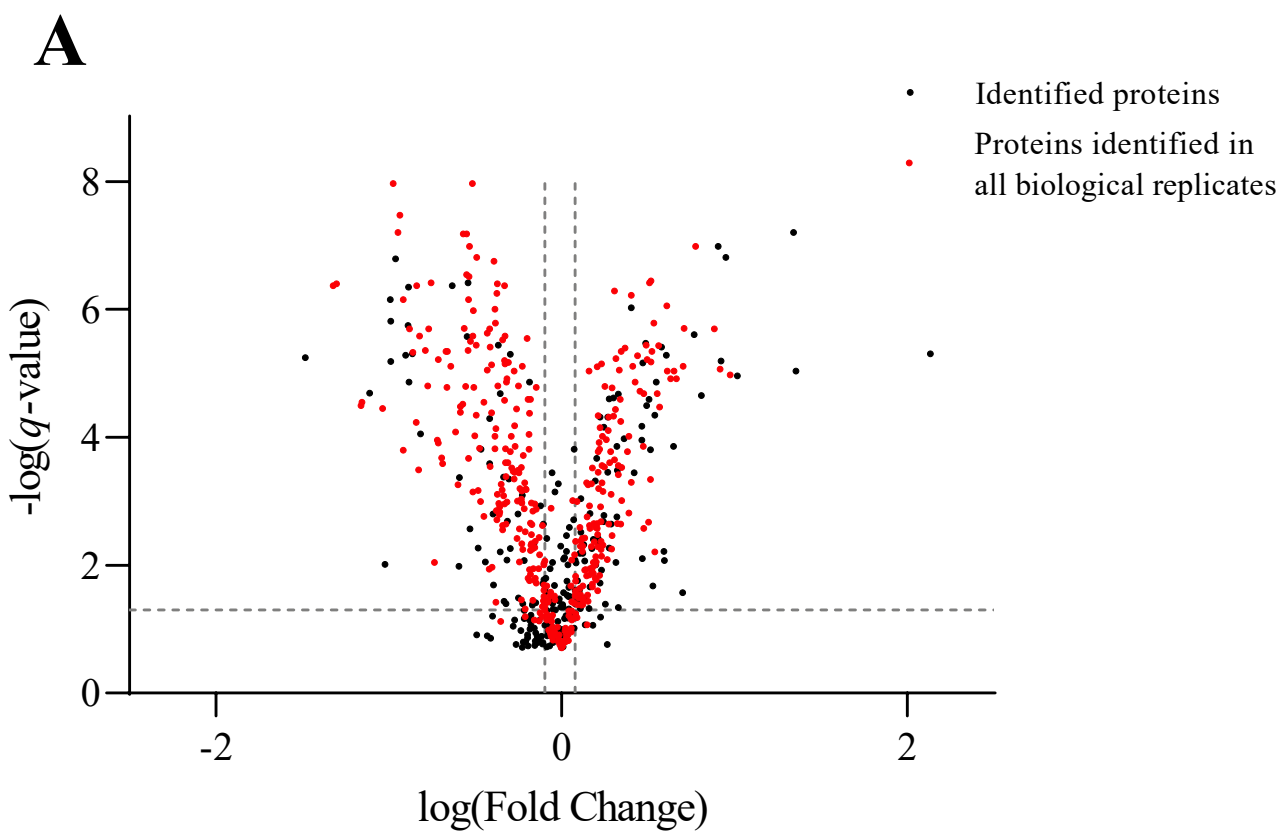
A
Identified proteins
Proteins identified in all biological replicates
-log(q-value)
log(Fold Change)
0
2
4
6
8
-2
0
2

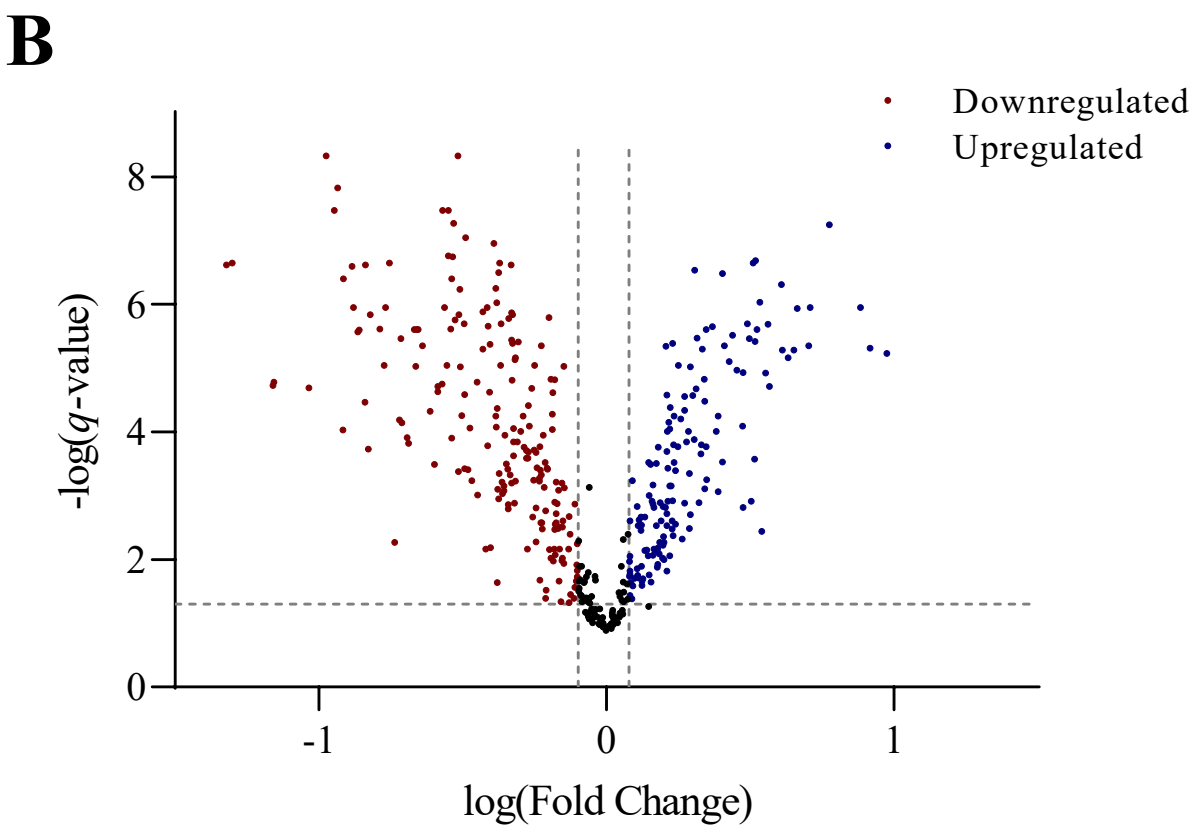
B
Downregulated
Upregulated
-log(q-value)
log(Fold Change)
0
2
4
6
8
-1
0
1

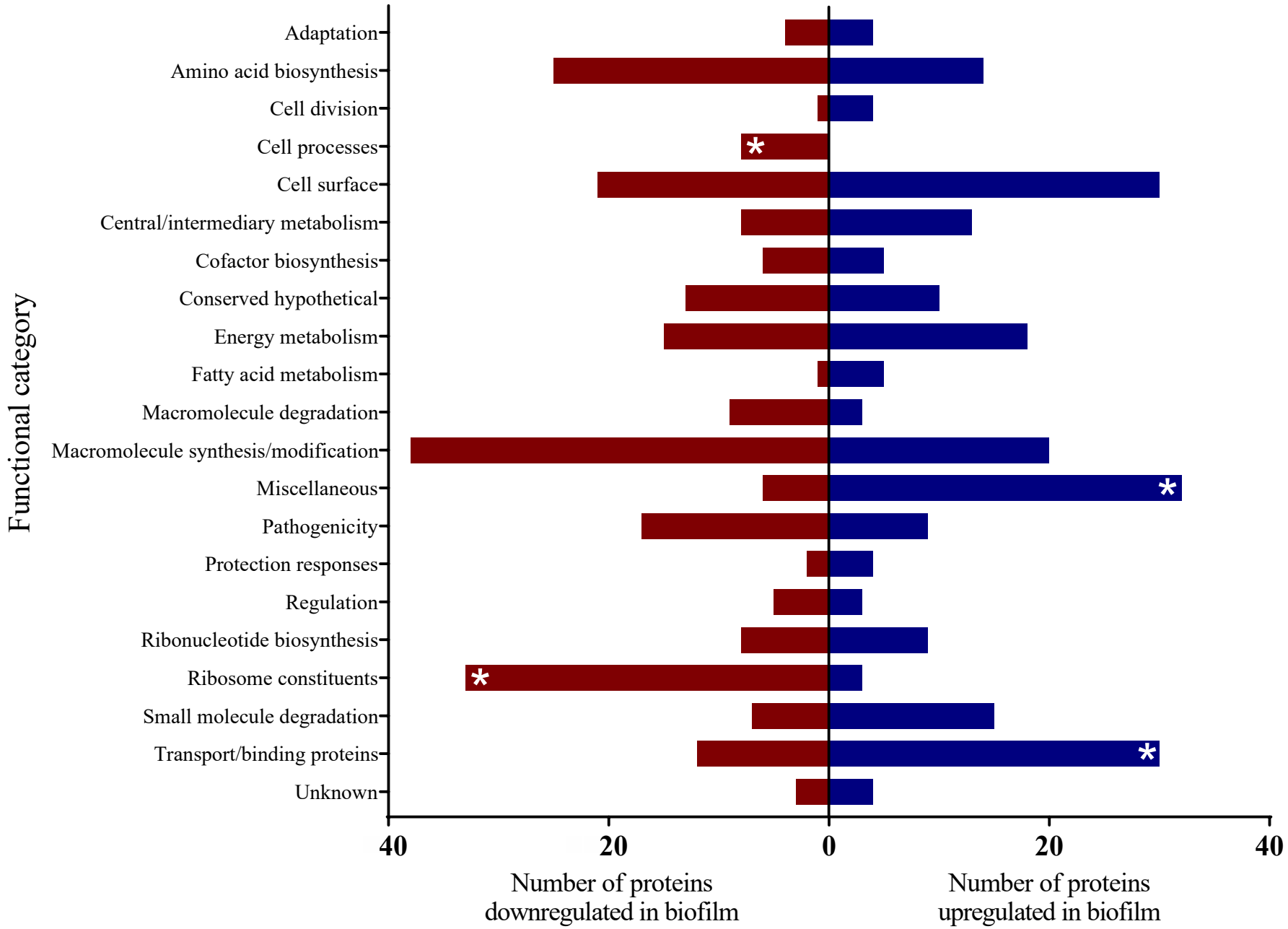
Functional category
Adaptation
Amino acid biosynthesis
Cell division
Cell processes
Cell surface
Central/intermediary metabolism
Cofactor biosynthesis
Conserved hypothetical
Energy metabolism
Fatty acid metabolism
Macromolecule degradation
Macromolecule synthesis/modification
Miscellaneous
Pathogenicity
Protection responses
Regulation
Ribonucleotide biosynthesis
Ribosome constituents
Small molecule degradation
Transport/binding proteins
Unknown
*
*
*
*
40
20
0
20
40
Number of proteins downregulated in biofilm
Number of proteins upregulated in biofilm

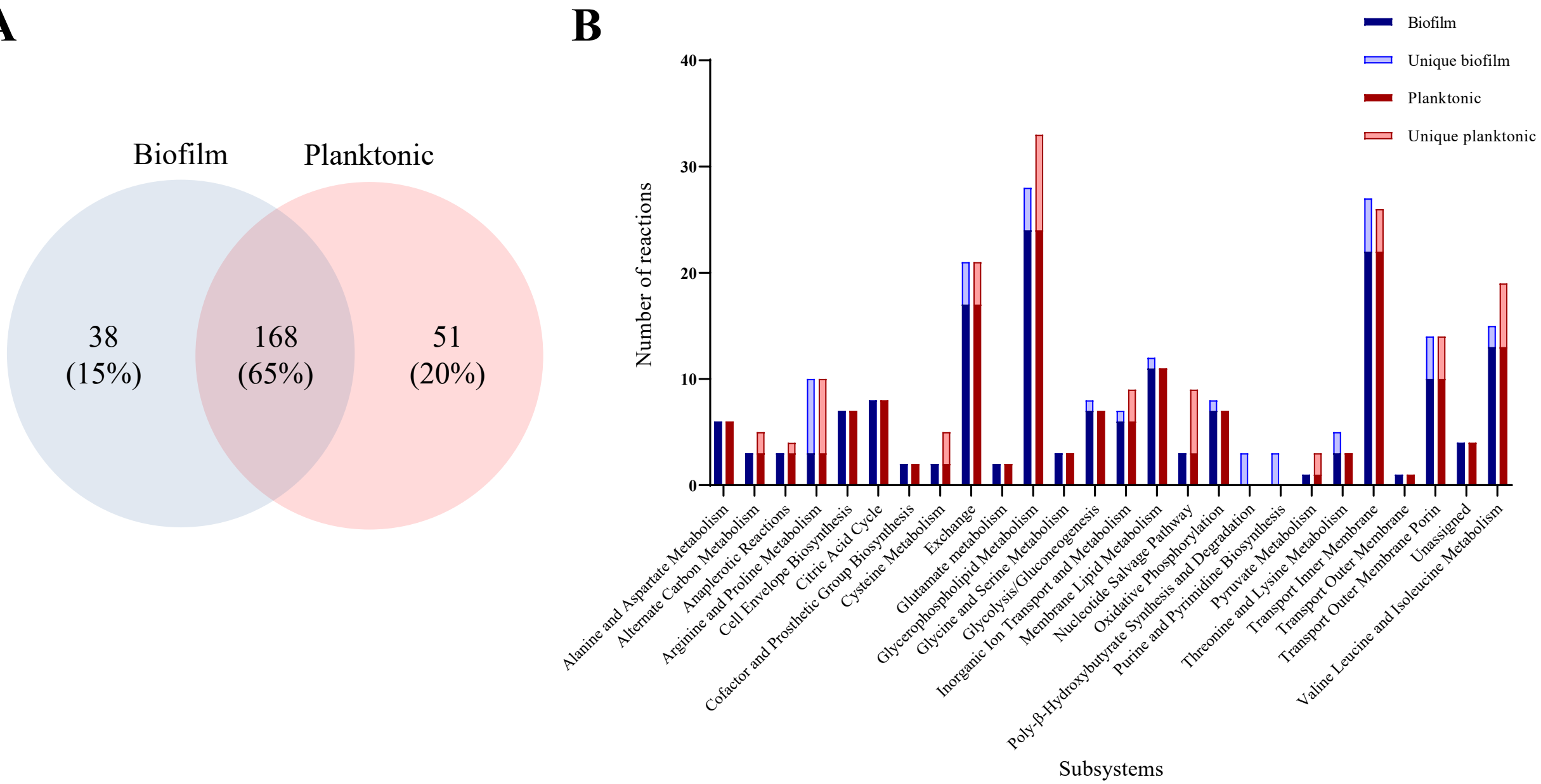
A
Biofilm
Planktonic
38
(15%)
168
(65%)
51
(20%)
B
Biofilm
Unique biofilm
Planktonic
Unique planktonic
Number of reactions
0
10
20
30
40
Alanine and Aspartate Metabolism
Alternate Carbon Metabolism
Anaplerotic Reactions
Arginine and Proline Metabolism
Cell Envelope Biosynthesis
Citric Acid Cycle
Cofactor and Prosthetic Group Biosynthesis
Cysteine Metabolism
Exchange
Glutamate metabolism
Glycerophospholipid Metabolism
Glycine and Serine Metabolism
Glycolysis/Gluconeogenesis
Inorganic Ion Transport and Metabolism
Membrane Lipid Metabolism
Nucleotide Salvage Pathway
Oxidative Phosphorylation
Poly-β-Hydroxybutyrate Synthesis and Degradation
Purine and Pyrimidine Biosynthesis
Pyruvate Metabolism
Threonine and Lysine Metabolism
Transport Inner Membrane
Transport Outer Membrane
Transport Outer Membrane Porin
Unassigned
Valine Leucine and Isoleucine Metabolism
Subsystems

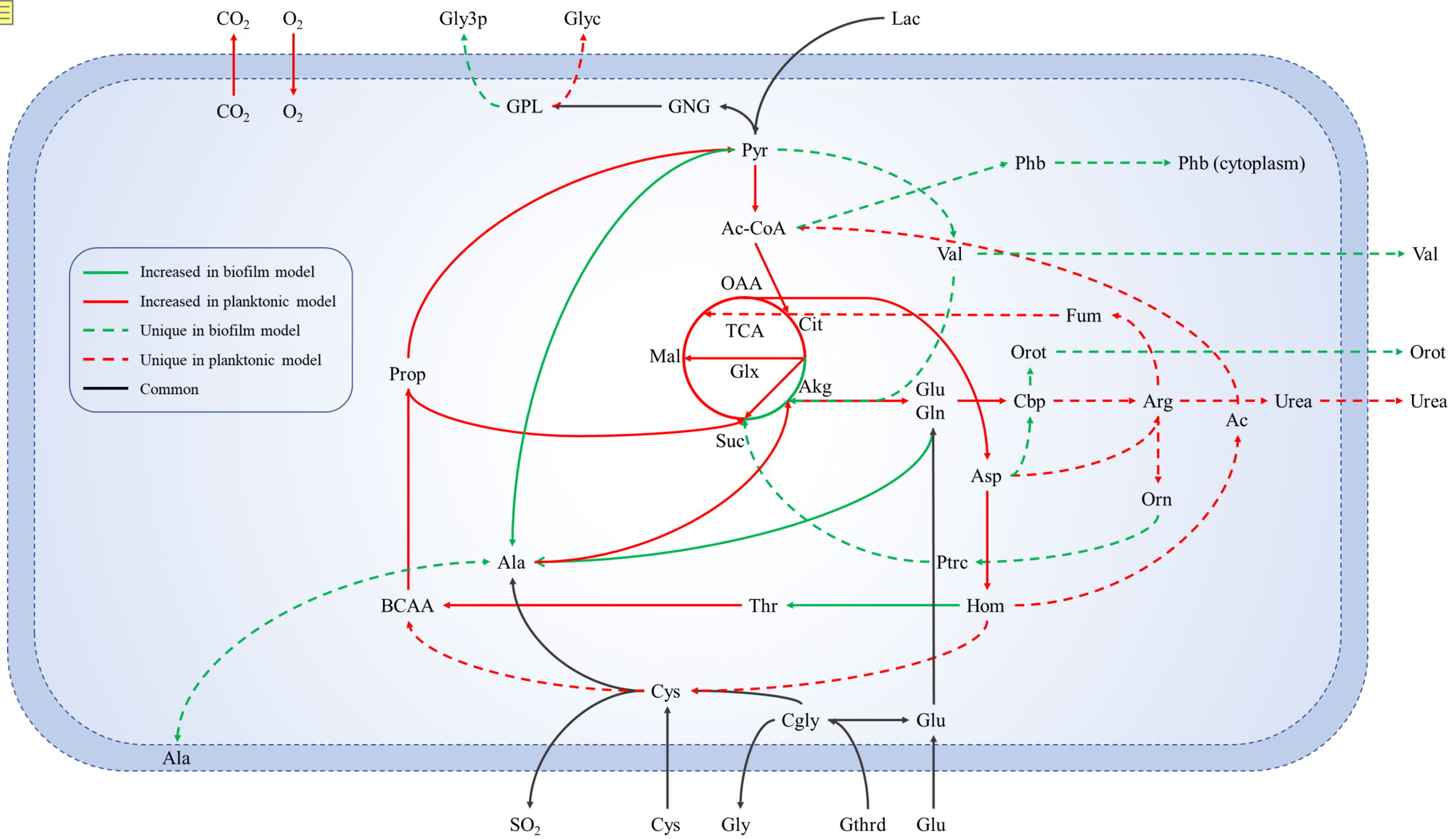
CO2
O2
CO2
O2
Gly3p
Glyc
Lac
GPL
GNG
Pyr
Phb
Phb (cytoplasm)
Ac-CoA
Val
Val
OAA
Fum
Cit
TCA
Mal
Glx
Orot
Orot
Prop
Akg
Glu
Gln
Cbp
Arg
Urea
Urea
Ac
Suc
Asp
Orn
Ala
Ptrc
BCAA
Thr
Hom
Cys
Cgly
Glu
Ala
SO2
Cys
Gly
Gthrd
Glu
Increased in biofilm model
Increased in planktonic model
Unique in biofilm model
Unique in planktonic model
Common